



# Evaluation of the p-11B reaction cross section through a silicon telescope in the 0.3–4.7 MeV range

D. Mazzucconi<sup>a</sup>, E. S. Bellotti<sup>b</sup> , D. Vavassori, D. Dellasega, S. Agosteo, M. Passoni, A. Pola, D. Bortot

Dipartimento di Energia, Politecnico di Milano, Via La Masa 34, Milan, Italy

Received: 3 February 2025 / Accepted: 8 May 2025

© The Author(s) 2025

Communicated by Alessia Di Pietro

**Abstract** The proton-boron fusion reaction  $^{11}\text{B}(p,\alpha)\alpha$  is of significant interest in nuclear physics, with implications in nuclear engineering, medicine, astrophysics, and fusion energy. Despite extensive research, understanding the reaction mechanism and kinematics remains elusive, underscoring the need for more experimental data. This study aims to quantify the p-11B reaction cross section across a proton energy range from 0.34 to 4.73 MeV. A novel experimental setup integrates custom-produced boron-coated targets with a two-stage monolithic silicon telescope for particle detection. The boron targets were fabricated using Pulsed Laser Deposition technique, allowing precise control over the target's properties. By utilizing a double-stage silicon device, accurate measurements of particle energy spectra were obtained, discriminating  $\alpha$  particles from scattered protons. The experimental campaign used a Van de Graff accelerator as a proton source. Monte Carlo simulations based on the FLUKA code assessed the actual reaction energy of primary protons. This study presents a novel proton energy-dependent cross-section behavior in the energy range from 0.34 to 4.73 MeV, including uncertainties on proton energy and cross-section values, along with detailed  $\alpha$  particle spectra at these energies. Comparison with literature data shows strong agreement for proton energies above the 0.675 MeV resonance peak, up to 3.5 MeV. A significant increase in the cross section close to 4.5 MeV indicates a potential unexplored resonance in this energy range. These findings suggest the need for expanding the energy range of cross-section evaluation and exploring possible resonances, particularly around 5 MeV.

## 1 Introduction

In the last years, the research related to the  $^{11}\text{B}(p,\alpha)\alpha$  reaction, denoted now on as the p-11B, gained renewed interest, since it could be relevant for different research areas. Among these, several efforts focused on medical and energy applications. Concerning the former sector, a treatment named Proton Boron Capture Therapy (PBCT) has been proposed as a possible strategy to improve conventional proton therapy. After initial theoretical and computational studies on PBCT [1–3], some experimental results showed a significant increase in the effectiveness of proton beam irradiation of  $^{11}\text{B}$ -containing cells [4–6], although the underlying radiobiological mechanisms have not been fully clarified [7–11]. Moving to energy applications, since decades the characteristics of the p-11B reaction are known to be appealing to conceive nuclear fusion schemes [12]. Indeed, unlike the well-known deuterium-tritium (DT) reaction, the p-11B one requires the use of abundant and stable isotopes and is aneutronic, potentially leading to a limited material activation and, in turn, to a low amount of radioactive waste. However, the p-11B requires a plasma temperature of approximately 300 keV, which is 30 times higher compared to the DT reaction [17], thus imposing several challenges for its practical use. Despite this, in the last years the scientific community has demonstrated a growing interest in this field, considering both laser-driven fusion [13–15] and magnetically confined fusion approaches [16, 18].

To assess the potential of the mentioned applications, detailed knowledge of a crucial experimental quantity such as the reaction cross section emerges as a fundamental step. In this respect, efforts have been performed in the last decades by increasing the proton energy. Moreover, measuring the cross section of a three-body nuclear reaction is inherently complex due to the continuous emission spectrum, which requires the ability to effectively discriminate between the

<sup>a</sup> e-mail: [davide.mazzucconi@polimi.it](mailto:davide.mazzucconi@polimi.it)

<sup>b</sup> e-mail: [emmasofia.bellotti@polimi.it](mailto:emmasofia.bellotti@polimi.it) (corresponding author)

produced particles and the incident ones. Most of available datasets focuses on proton energies  $E_p$  ranging from 10s to 100s of keV up to 4 MeV [19–30], considering both the cross section related to single reaction channels or the total one. On the contrary, information concerning higher proton energies can be found in fewer publications [22,31,32]. Moreover, independently of the specific proton energy, discrepancies can be observed between the literature data both in the energy scale and cross section values [21,33], mainly attributable to the different approaches adopted for removing the contribution of primary protons scattered by the target to the measured spectra: the use of thin metallic foils as filters [24–26], the adoption of specific detector configurations [21,22,24] or the reconstruction of the low-energy region by means of theoretical assumptions [19,27,29]. Moreover, some results were obtained with a limited characterization of boron target properties, often retrieved indirectly during or after the experiments [26,28,34].

In this scenario, more robust and reliable  $\alpha$  particle spectra and cross section data over a relatively large range of proton energies are needed to achieve a better understanding of the reaction physics through the development of proper models related to reaction mechanism [35,36] or the benchmarking of simulation tools such as the Monte Carlo code FLUKA [37,38]. In addition, also the abovementioned applications can benefit. As an example, in the context of nuclear fusion, the appearance of more accurate cross section measurements by Sikora et al. [29] has allowed for a recalculation of fusion reactivity which resulted 20–30% higher than the one computed previously [39,40].

This work deals with an extensive investigation of the  $p$ -11B reaction carried out with the novel experimental strategy recently published by the research group [41]. The measurement set-up consists of a two-stage monolithic detection system, able to discriminate different types of particles impinging on it, and well characterized boron-coated targets, properly re-designed to avoid the limitations emerged in [41]. Both enriched boron-11 and natural boron targets were irradiated, and the impinging proton energy was tuned in the range 0.3–5 MeV. Thanks to the peculiarities of the detector, the total energy distribution of the generated  $\alpha$  particles has been measured by means of an event-by-event discrimination of scattered primary protons. This allowed for precise calculation of the reaction cross section, without any analytical assumption or extrapolation.

## 2 Materials and methods

The present description of the physics of the reaction is based on a two-step process [42]. The interaction of the proton with the  $^{11}\text{B}$  nucleus (the Coulomb barrier of the system is estimated equal to 1.55 MeV [43]) forms a  $^{12}\text{C}^*$  compound

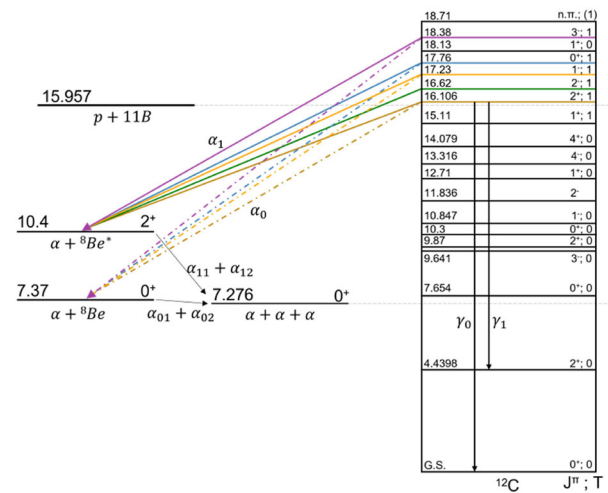


**Fig. 1** The reaction scheme for five excited states of  $^{12}\text{C}$  is shown. The arrows indicate the possible decay channel ( $\alpha_0$  or  $\alpha_1$ ) according to the conservation of angular momentum and parity

nucleus in one of its excited states according to the incident proton energy [44]. The decay of the  $^{12}\text{C}^*$  nucleus is modelled as a sequence of a two-breakup process in which the  $^{12}\text{C}^*$  nucleus first produces a primary  $\alpha$  particle and a  $^8\text{Be}$  nucleus ( $^{12}\text{C}^* \rightarrow \alpha_{prim} + ^8\text{Be}$ ) that, in turn, breakups into two secondary  $\alpha$  particles ( $^8\text{Be} \rightarrow \alpha_{sec,1} + \alpha_{sec,2}$ ). As shown in Fig. 1, in the first step, the  $^8\text{Be}$  nucleus can be produced in its ground state ( $J^\pi = 0^+$ ) or in its first excited state ( $J^\pi = 2^+$ ), which are referred to as the  $\alpha_0$  channel and  $\alpha_1$  channel, respectively. For proton energies in the range  $E_p = 0.1 \div 3$  MeV, the reaction has been experimentally investigated and, using the two-step model, the breakup of different  $^{12}\text{C}$  states (16.11, 16.62, 17.23, 17.76 and 18.38 MeV) has been described [19–28,34,42,45–49].

Nonetheless, some discrepancies and open points are still present. As far as how the  $\alpha_1$  channel reaction proceeds at the resonance  $E_p = 0.675$  MeV is concerned, a complete understanding of the break-up mechanism seems to be missing. Indeed, in more recent works, some authors report that the primary  $\alpha$  particle should have orbital angular momentum  $l$  equal to 1 [26], while other authors report  $l = 3$  [28,49] or a mixture of the two in agreement with the findings of previous works [34]. Thus, it is evident that further efforts are needed for a complete comprehension of the reaction, also in view of the discussed applications. Specifically, the availability of reliable experimental data about fundamental quantities (e.g., cross section,  $\alpha$  particle-proton ratio,  $\alpha$  particle spectrum) is crucial. In this framework, the development of the experimental set-up is fundamental.

Experimental works focus on the measurement and analysis of  $\alpha$  particle energy spectra. At  $E_p \approx 0.6$  MeV, results show a sharp  $\alpha$  peak around 6 MeV, assigned to the primary of  $\alpha_0$  channel, and a broad peak around 4 MeV, assigned to the

primary of  $\alpha_1$  channel [28]. These values increase by increasing the energy of incident protons. This is the experimental evidence in the high-energy part of the measured  $\alpha$  spectra. However, as already stressed in earlier works [24], if the low-energy part is considered, the interpretation is not straightforward, due to the presence of protons elastically scattered by the target. To overcome this issue, some authors adopted multiple single-stage detectors in coincidence [24, 42, 47, 48]. Results stress the presence of a contribution in the low-energy region associated to the secondary particles of the  $\alpha_0$  channel. Specifically, the coincidence spectrum measured by Laursen et al. [42] show a contribution in the low-energy region (1–2 MeV). According to the authors, this is originated from triple coincidence events mainly related to the  $\alpha_0$  channel. This is also in agreement with modeled spectra reported in [29, 49]. Nevertheless, results derived so far need further investigations and refinements.

An important role in the experimental investigation is played by the adopted boron targets. In previous works, boron targets were mainly produced by electron beam evaporation, both as self-supporting foils and as films deposited over different kind of substrates (e.g., carbon, aluminum, tantalum, silver). The estimation of the target mass thickness was usually performed during or after the experiments by indirect methods [34, 48], though its direct measurement could represent an improvement. Indeed, as underlined in [21] and [27], proper characterization of the target thickness, as well as other properties such as density and chemical composition, is important both to obtain accurate information and in view of simulation campaigns aimed at interpreting measured data. Moreover, the exploitation of a different deposition technique that allows significant variation in the target's mass thickness, depending on the physical quantity being investigated, could represent a further step forward.

Targets constituted by a metallic substrate and a boron (B) layer were irradiated during experiments. Specifically, the production of targets with a layer made either of natural Boron isotopic enriched  $^{11}\text{B}$  was carried out.

As far as the substrate is concerned, a commercial mechanical rolled aluminium (Al) foil with a thickness of  $2.4\ \mu\text{m}$  was employed, corresponding to a mass thickness of  $650\ \mu\text{g}/\text{cm}^2$ . A rectangular stainless-steel holder was exploited as support for Al foils, as shown in Fig. 2a. The holder featured holes, each measuring 1.5 mm in diameter, allowing the proton beam to pass through. Al foils were fixed over the holes.

### 2.1 Boron targets

Considering the B layer, a thickness of about 500 nm was identified as the best compromise between a low energy spread of  $\alpha$  particles and a sufficiently high reaction yield. To this end, a natural B or isotopic  $^{11}\text{B}$  target was ablated

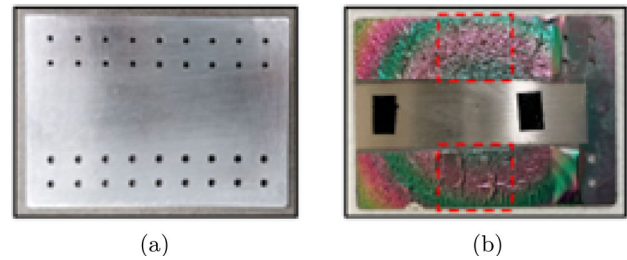


**Fig. 2** **a** Picture of the perforated support used to produce the targets. **b** Picture of a representative irradiated target. Areas enclosed by red dashed lines were exploited during irradiations experiments. A Si substrate was placed in correspondence of the central shadow for characterization analyses

exploiting a ns-Pulsed Laser Deposition (PLD) system [50] to grow a film on the previously described substrate. Before the ablation process, the vacuum chamber was pumped down to  $8 \cdot 10^{-3}$  Pa. During the film deposition, the laser pulse energy ranged between 700–750 mJ, resulting in a laser fluence varying between  $8\text{--}8.5\ \text{J}/\text{cm}^2$  (assuming a laser spot area on the ablated target equal to  $8.8\ \text{mm}^2$ ). Moreover, the target-to-substrate distance was fixed to 9 cm and, to improve the uniformity of the film, a horizontal shift between the substrate and the target was introduced. In this respect, a single side polished  $500\ \mu\text{m}$  thick (100) Si wafer was placed at the center of the stainless-steel holder for proper characterization and to evaluate the effective B film thickness.

Figure 2b shows the realized target. Due to the film's residual stresses, the target exhibits the formation of corrugations. To precisely analyze the morphological features and thickness of the B film, a Supra 40 Scanning Electron Microscope (SEM) with an accelerating voltage of 5 kV was used. As illustrated in Fig. 3a, the planarity of the target appeared adequate. This is confirmed also by higher magnification images (see Fig. 3b, c) which highlight a low amount of surface droplets and aggregates on the film surface. Moreover, the circular-coloured fringes visible in Fig. 2b on Al foils indicated a film thickness variation over the support area. Thus, only the areas enclosed by red dashed lines in Fig. 2b were considered for irradiations experiments. The B film thickness in this region was estimated using the analysis of the Si substrate. In contrast, film composition and density were retrieved by Energy Dispersion X Ray Spectroscopy (EDX) measurements [51] directly performed on the B layer grown on the Al substrate. Specifically, the mass thickness of the B film was estimated by multiplying the thickness and density measured as previously described. The film properties are summarized in Table 1.

It should be noted that the detailed characterization of the B targets in terms of thickness, density and composition is fundamental for a reliable evaluation of the reaction cross section. Indeed, measurements were conducted on both targets, with several taken at the same proton energy for direct

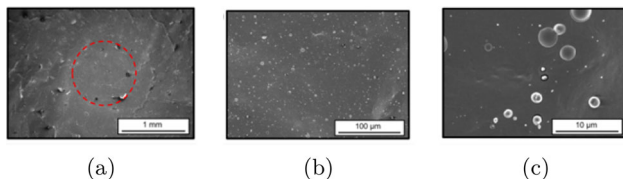


**Fig. 3** **a** SEM plane image of natural B films deposited onto Al foil fixed on a perforated holder. The hole position is highlighted by the dashed circle line. **b, c** Higher magnification SEM plane micrographs showing a low presence of droplets and aggregates on target surface

**Table 1** Thickness, composition, density and mass thickness of deposited natural B and  $^{11}\text{B}$  films. Magnesium (Mg) is present as impurity in the ablated natural B target

B layer /substrate	Effective thickness [nm]	Atomic Fraction B, O, Mg	Density [ $\text{g}/\text{cm}^3$ ]	Mass Thickness [ $\mu\text{g}/\text{cm}^2$ ]
Natural B /Al foil	501.7 $\pm 71.5$	$87.3 \pm 2\%$ 11.1% 1.6%	2.35 $\pm 0.2$	118 $\pm 20$
$^{11}\text{B}$ /Al foil	457.27 $\pm 27.0$	$84.7 \pm 2.2\%$ 15.3% —	2.289 $\pm 0.06$	105 $\pm 6.8$

comparison. Necessary corrections were applied, including adjustments for composition, density, and mass thickness for the natural B target. After a detailed comparison of the spectra, counts, and cross sections obtained from both targets irradiated at the same proton energy, the results were found to be comparable. Therefore, from this point onward, no distinction between the two targets will be made in the analysis.

## 2.2 The double-stage silicon telescope

The double stage detector adopted for the experimental set-up is based on a monolithic silicon telescope (MST) (see 4) [41,52]. The two stages, called  $\Delta E$  and E, are  $1.9\ \mu\text{m}$  and a  $500\ \mu\text{m}$  thick, respectively, with a sensitive area of  $1\ \text{mm}^2$ . Both stages are collected separately by two different electronic chains. Signals are acquired by a two-channel ADC in coincidence mode to keep the time correlation between the E and  $\Delta E$  events. The time resolution of the coincidence was  $1\ \mu\text{s}$  for minimizing the pile up probability. The telescope allows physical discrimination of the type of the impinging particle by processing the bi-variate distribution of events, i.e. by elaborating the so-called “ $\Delta E$ -E scatter-plot”. The energy calibration of the system has been carried out and verified through different  $^{241}\text{Am}$  sources.

The discrimination performed by the silicon telescope offers the possibility of distinguishing, event-by-event, scattered primary protons from  $\alpha$  particles generated in the p- $^{11}\text{B}$  reactions and, therefore, deriving spectra of  $\alpha$  particles

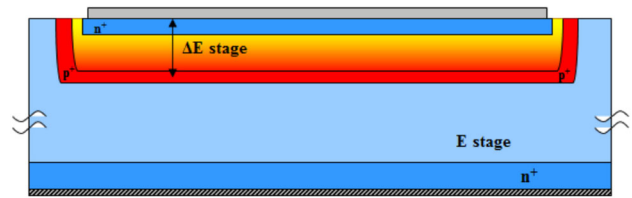


**Fig. 4** Scheme of the monolithic silicon telescope

or protons only. More details about the detector and its use for discrimination can be found in [41]. The capability of distinguishing protons from  $\alpha$  particles offers the unique possibility of deriving an  $\alpha$  particle distribution without any assumption on the low energy region of the spectrum, which can be highly distorted by the presence of the primary scattered protons.

## 2.3 Experimental set-up

The experimental campaign was carried out at the 7 MV CN Van de Graaff accelerator of the INFN - Laboratori Nazionali di Legnaro (LNL) in Legnaro, Italy. The targets and the silicon telescope were assembled on a specific support, facing each other, and placed into a sealed vacuum chamber positioned along the  $0^\circ$  beamline of the accelerator. The accelerated proton beam was shaped with a circular aluminium collimator with a diameter of 1 mm. The beam current was kept around 1 nA with a maximum 10% variation. The beam current and the integral charge were measured through a Faraday cup placed downstream of the target and connected to an electrometer which records the value of the current for each second. The total number of protons has been calculated by integrating the current measurements and its uncertainty has been evaluated by considering the accuracy of the electrometer only, which is equal to the  $0.05\% \times \text{Reading} + 2\ \text{pA}$ . For verifying the performance of the Faraday cup in determining the correct number of protons, some experimental tests have been performed by placing and removing the target by moving its support. No significant variations on the beam current have been detected. The described configuration was adopted for maximizing the rate of the detected  $\alpha$  particles for studying the reaction process. A scheme of this experimental set-up is reported in Fig. 5. The silicon telescope was placed at  $30\ \text{mm}$  ( $\pm 0.2\ \text{mm}$ ) from the center of the target at a  $60^\circ$  angle with respect to the proton beam axis. Therefore, the solid angle covered by the detector is equal to  $1.11 \times 10^{-3}\ \text{sr}$ .

In order to estimate accurately the actual energies that protons possess at the entrance of the boron target, Monte Carlo simulations based on FLUKA code have been performed. More specifically, to be as close as possible to the experimental conditions, the actual proton energies at the entrance of the boron target were iteratively calculated to reproduce

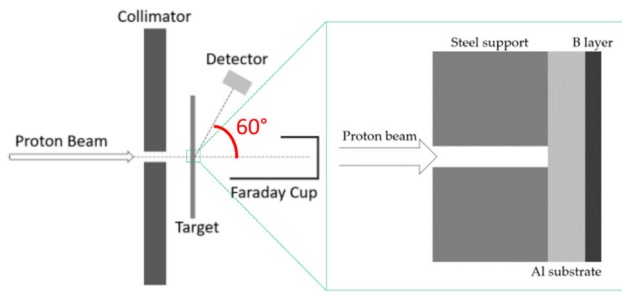


**Fig. 5** Sketch of the experimental set-up (left side) and details of the target (right side). The image is not in scale

at best the distribution of scattered protons measured at  $60^\circ$  by the MST.

The capability of the silicon telescope at discriminating protons from  $\alpha$  particles was exploited also for verifying the proton energy given by the accelerator, which could be source of high uncertainty as underlined by Munch et al. [21]. This task was performed by comparing the energy of the elastically scattered protons with the same energy calculated via Monte Carlo simulation by exploiting the FLUKA code.

The comparison between the experimental distribution of scattered protons and those obtained through Monte Carlo simulation provided an estimation of the uncertainty on the energy impinging on the boron target. This uncertainty was derived from the FWHM of the elastically scattered experimental proton peak with respect to the simulated one. Proton energies mentioned in the following are referred to as those tuned with the FLUKA simulations instead of the nominal acceleration energies. The corresponding list of the tuned energies is provided in Table 2. It should be noted that the goal of the FLUKA Monte Carlo simulations was to tune the proton energy only and not to compare the number of scattered particles. Moreover, the simulations do not take into account other effects, such as detector resolution and the presence of the vacuum chamber.

#### 2.4 Cross section evaluation and uncertainty estimation

Reaction cross sections were assessed for the two different channels of the  $p\text{-}^{11}\text{B}$  reaction. The differential reaction cross section  $d\sigma/d\Omega$  was computed as:

$$\frac{d\sigma}{d\Omega} = \frac{\text{Counts}}{N_t N_p d\Omega}$$

where  $N_t$  is the number of  $^{11}\text{B}$  nuclei per  $\text{cm}^2$  in the target,  $N_p$  is the number of incident protons, and  $d\Omega$  is the solid angle subtended by the detector.

The capability of the silicon telescope at discriminating  $\alpha$  particles from protons allows the calculation of the reaction cross section by exploiting experimental data only, thus avoiding other assumptions. This approach is strongly dif-

ferent with other measurement techniques in which a single stage detector is used. In those cases, a model is used to guess the low-energy part of  $\alpha$  spectra (which fall under the scattered protons distribution) [29].

The calculation of the total reaction cross section values at each energy was performed by processing measured spectra by considering all measured counts related to  $\alpha$  particles. Whereas, the calculation of the  $\alpha_0$  channel has been performed by considering the counts under the higher energy peak in the spectrum.

The uncertainty on the reaction cross section values reported in the following was calculated by considering the number of detected  $\alpha$  particles, the relative distance between the target and the detector, the target mass thickness and composition, and the integrated proton beam charge. All the sources of uncertainty related to the target are listed in Table 1 while the others in Section 2.3.

### 3 Results and discussion

#### 3.1 Scatter plots and proton- $\alpha$ discrimination

The  $\Delta E$ - $E$  scatter-plots obtained for irradiations with 0.69 and 4.65 MeV protons are shown in Fig. 6. As a reference, the theoretical  $\Delta E$ - $E$  distribution of protons and  $\alpha$  impinging normally on the detector (red and black lines respectively) are also reported.

Two main contributions can be observed: protons elastically scattered by the target and its support (events around the black line) and  $\alpha$  particles (events around the red line). To discriminate between protons and  $\alpha$  particles, a threshold can be set between the two theoretical curves, such that most  $\alpha$  particles are above it while protons are below. In Fig. 6, the selected threshold is represented in yellow and consists of a piecewise function that mimics the behavior of the theoretical curves. The two populations are well separated, effectively discriminating the energy spectra of  $\alpha$  particles from protons.

The benefit of using the MST is evident in Fig. 7, where energy spectra of  $\alpha$  particles and scattered protons are plotted separately after the application of the discrimination procedure. If a single stage detector was used, many events pertaining to  $\alpha$  particles would be hidden by scattered protons. This effect strongly depends on the energy of primary protons: the higher is the proton energy, the greater the portion of the  $\alpha$  particle spectrum that would be hindered by a single stage detector. This effect is clearly shown in Fig. 7b, where the overlapping between proton and  $\alpha$  particle spectra is more significant for protons at 4.65 MeV. Although the discrimination is more effective at higher energies, even at low ones, e.g. 0.69 MeV protons (see Fig. 7a), it is evident that a portion of the  $\alpha$  particle spectrum would be lost without it. This emphasizes that the need for the double-stage detector is not

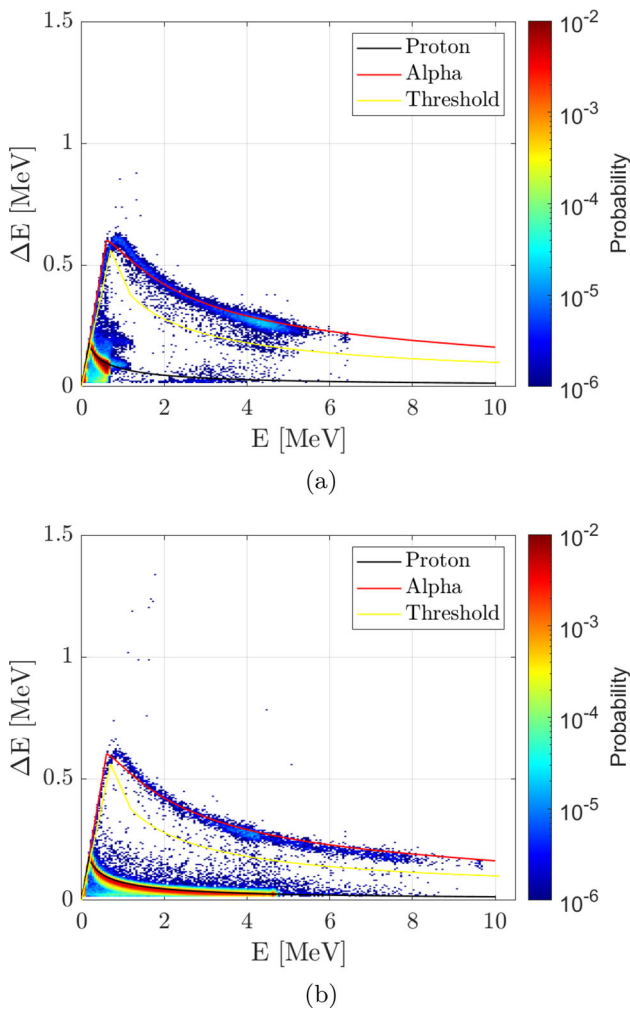


**Fig. 6** Scatter-plots related to the proton and  $\alpha$  signals. The two plots refer to 0.69 MeV (a) and 4.65 MeV (b)

limited to higher energy protons, but even at lower energies, it ensures a more accurate separation of particles and prevents valuable data from being lost.

### 3.2 $\alpha$ particles energy distribution

Spectra of  $\alpha$  particles produced by the p-11B reaction at primary proton energies from 0.34 MeV up to 4.73 MeV are shown in Fig. 8, where all energy values, referred to the center of mass system, are those estimated through FLUKA Monte Carlo simulations. Moreover, all spectra shown in Fig. 8 are normalized to the number of the  $\alpha$  particle counts, therefore to unit area and, for this reason, the y-axis is presented in terms of probability.

As expected, the  $\alpha$  particle distributions shift towards higher energies with increasing impinging proton energy. The spectra reveal three distinct contributions: a peak associated to the  $\alpha_1$  channel, a peak related to the  $\alpha_0$  channel, and

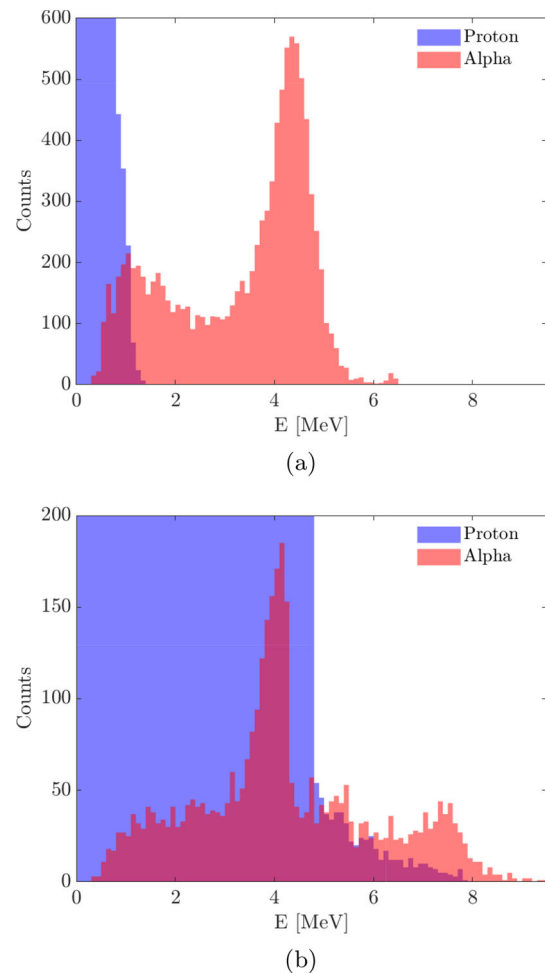


**Fig. 7** Energy spectra of  $\alpha$  particles and scattered protons after the application of the discrimination procedure. Primary proton energies are 0.69 MeV (a) and 4.65 MeV (b)

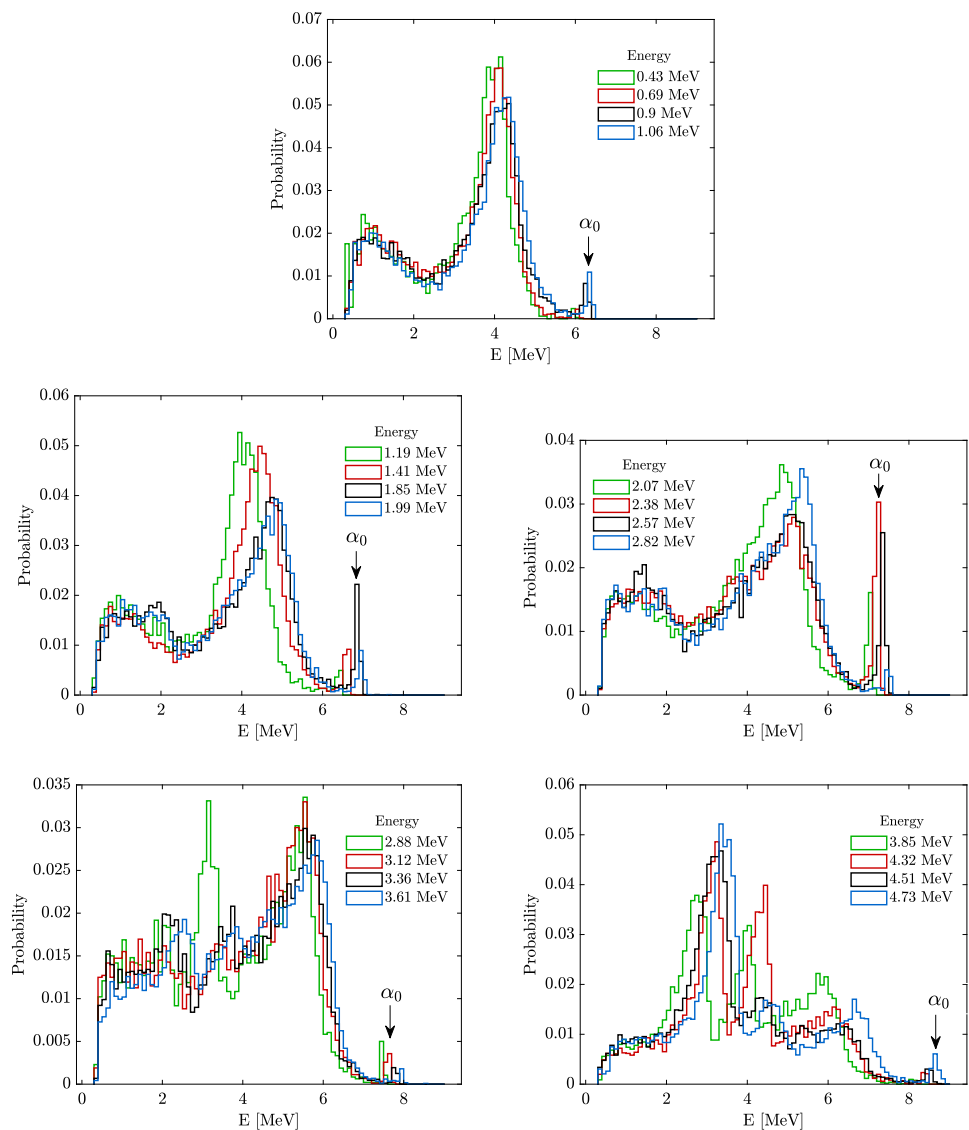
a low-energy distribution attributed to the decay of the  $^8\text{Be}$  nucleus.

The primary contribution to the spectra is a distribution peaking at energies ranging from approximately 4.5 MeV to 7 MeV for proton energies between 0.34 MeV and 4.73 MeV. This distribution is consistent with  $\alpha$  particles generated via the  $\alpha_1$  channel.

The contribution from  $\alpha$  particles associated with the  $\alpha_0$  channel is characterized by a well-defined high-energy peak, with peak intensity which vary across different proton energies. Notably, higher peaks are observed for a proton energy between 1.85 and 2.57 MeV.

The low-energy distribution, which becomes more pronounced at higher proton energies, is consistent with secondary  $\alpha$  particles emitted from the decay of the  $^8\text{Be}$  nucleus (for both reaction channels). This confirms previous models [47] and experimental results obtained using coincidence techniques [42]. It is important to note that this distribution cannot be measured with a single-stage detector.

**Fig. 8** Measured  $\alpha$  particle energy spectra for proton energies in the range 0.34–4.73 MeV. All spectra are normalized to unit area



For some proton energies (i.e., 2.88, 3.85, 4.32, 4.51, and 4.73 MeV), the measured  $\alpha$  particle distributions reveal additional energy peaks. A possible explanation for these peaks is the alpha emission from the  $^{27}\text{Al}(p, \alpha)^{24}\text{Mg}$  reaction on the aluminum support. This reaction has a noteworthy cross section in the considered proton energy range characterized by some resonances. Moreover, due to the thickness of the aluminum support compared to the boron target, this parasitic reaction may contribute to the detected alpha yield. As the contributions from the two reactions cannot be discriminated, this non-trivial behavior is certainly worthy of further measurements.

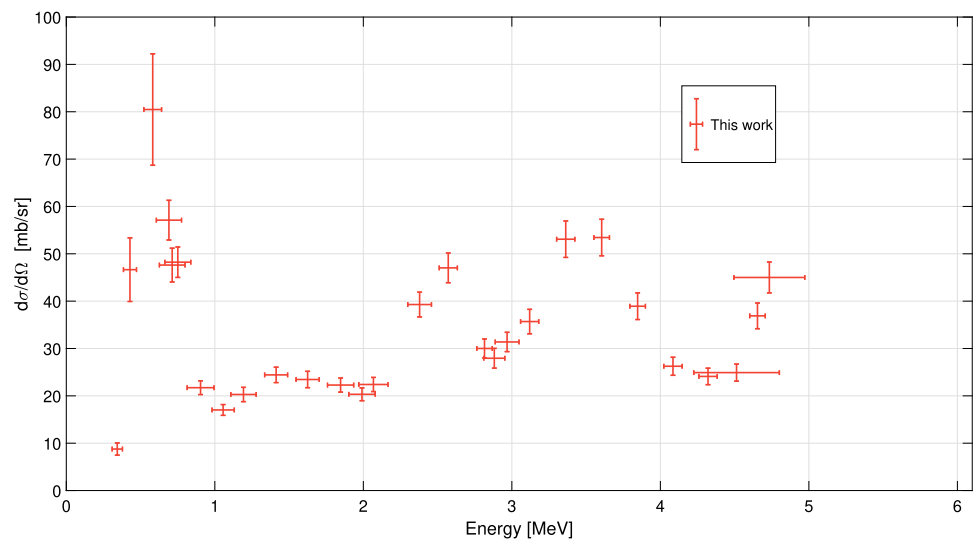
### 3.3 Cross section evaluation

The results obtained at various proton energies are listed in Table 2 and visually represented in Fig. 9. The data are dis-

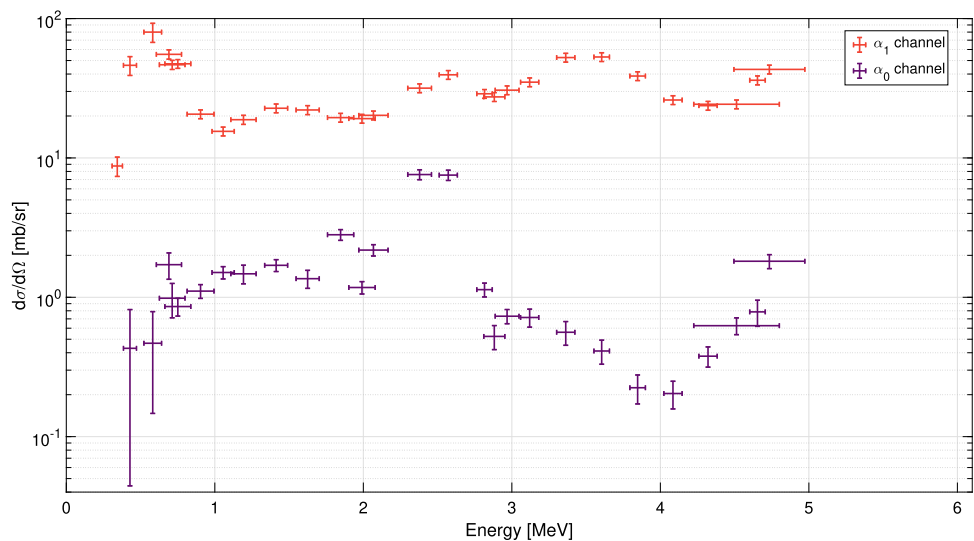
played with corresponding uncertainties. Figure 9 presents both the total differential cross section (Fig. 9a) and the partial differential cross section for  $\alpha_0$  and  $\alpha_1$  channels (Fig. 9b). In addition, a comparison with data from the literature is included in Fig. 10 to provide context and compare the current findings. The large error bars observed at 4.73 and 4.51 MeV are due to a broader peak in the experimental proton spectra. As a result, applying the procedure described in Section 2.3 leads to higher energy uncertainty values.

Figure 10a presents the differential cross section at  $60^\circ$  compared with data from Sikora et al. [29] measured at the same angle. This comparison underlines the reliability of the presented dataset at the measured angle. Taking into account the associated uncertainties, the trend of the two differential reaction cross section is generally in good agreement, with the exception of the resonance peak observed around 670

**Fig. 9** Differential reaction cross section measured at  $60^\circ$  for different proton energies. **a** Total differential cross section. **b** Partial differential cross section for  $\alpha_0$  and  $\alpha_1$  channel



(a)



(b)

keV. Notably, the resonance peak in Sikora et al. [29] data appears higher.

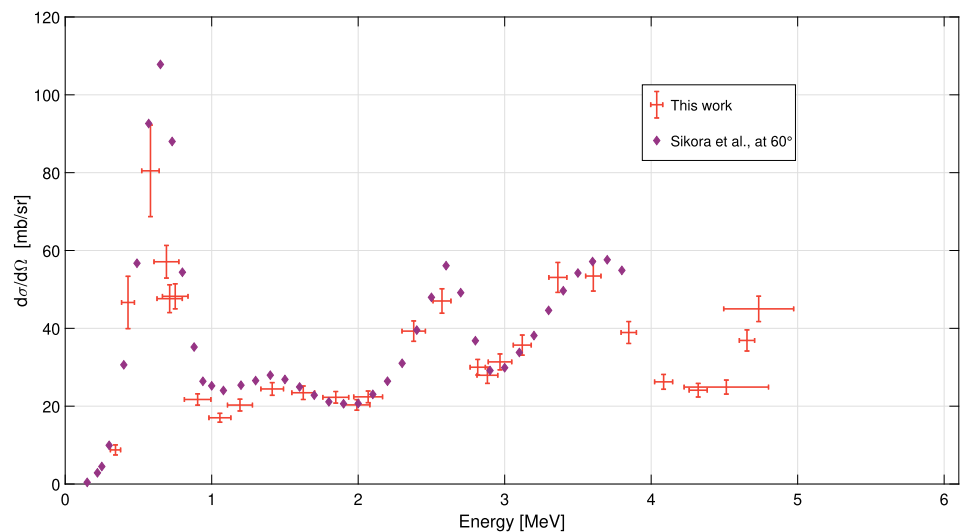
To provide a more comprehensive comparison with the available literature data, the differential cross section was integrated over the total solid angle, by assuming an isotropic emission. The results are presented in Fig. 10b. Although the emission has been shown to be non-isotropic [21], mainly for the  $\alpha_0$  channel, the work by Spraker et al. [28] shows that the total emission on the 675 keV resonance can be considered isotropic while a 25% anisotropy can be seen on the 2.64 MeV resonance only. In the remaining energies in the range 0.15–3.8 MeV a maximum 5% deviation from isotropy has been found. Moreover, the data from [29] show that the differential cross section at  $60^\circ$  closely represents the average

value, making the described approach acceptable within the uncertainty values.

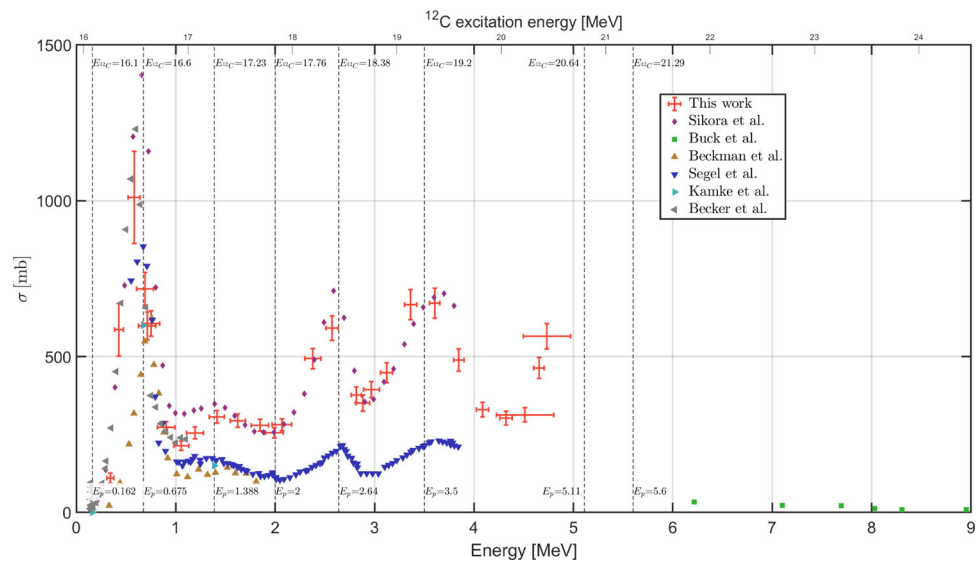
This comparison demonstrates a strong agreement between the current measurements and previously published data. Specifically, the general trend of the total reaction cross section aligns well with the results of Sikora et al. [29], with the exception of the resonance peak observed around 670 keV (Fig. 10b). The coherence of this comparison with respect to the one depicted in Fig. 10a strongly supports the previously described assumption on the total cross section evaluation.

Instead, in the region of the main resonance the results of this work are in better agreement with Becker et al. [26] which show a cross section around 1.2 b. The experimental cross section derived by Becker et al. [26] was obtained using

**Fig. 10** Reaction cross section measured at different proton energies (red) compared with experimental cross section from literature. **a** Differential cross section measured at  $60^\circ$  compared to the results from Sikora et al. [29] at the same angle. **b** Total reaction cross section compared with experimental total cross section from literature [19, 23, 24, 26, 29, 32]



(a)



(b)

complex coincidence techniques, which provide more reliable proton-alpha discrimination. This highlights the critical importance of efficient proton-alpha discrimination in studying this reaction. This discrepancies may be attributed to the fact that the adopted proton energies do not match exactly the resonance value, which is considered at 675 keV.

Figure 10b further compares the results of this study with other cross-section data available in the literature [19, 23, 24]. This comparison highlights a separation into two distinct groups for proton energies above 1 MeV. Specifically, the present results, along with those reported by Sikora et al. [29] and Becker et al. [26], show higher cross section values compared to the data from Beckman et al [19], Segel et al. [23] and Kamke et al. [24]. This discrepancy may be attributed to two possible reasons: the angle at which the data were

measured and the assumptions made for selecting the alpha related signals. Firstly, Beckman et al. [19] evaluated the total cross section by integrating over the solid angle the measurements at  $97^\circ$ . Secondly, in [19, 23, 24], different hypothesis have been made for the discrimination between proton and alpha particles, therefore not all the events measured in the spectra are used for the evaluation of the cross section. In contrast, since the alpha energy spectra were extrapolated down to zero using a model, Sikora et al. [29] were able to consider the full alpha spectrum in the cross section evaluation.

It must be underlined that all the literature results presented in Fig. 10 lack any indication of experimental uncertainty, which is crucial for making more detailed comparisons. Finally, Fig. 10 reveals a significant increase in the cross section near 4.5 MeV, which likely indicates the pres-

**Table 2** Differential reaction cross section measured at 60° listed with the correspondent proton energies. Results are reported with associated uncertainties

Energy on Boron [MeV]	$d\sigma/d\Omega$ [mb/sr]		
	$\alpha_0$ channel	$\alpha_1$ channel	Total CS
4.73 ± 0.239	1.81 ± 0.21	43.2 ± 3.1	45.0 ± 3.3
4.65 ± 0.052	0.79 ± 0.17	36.1 ± 2.7	36.9 ± 2.7
4.51 ± 0.288	0.63 ± 0.09	24.3 ± 1.8	24.9 ± 1.8
4.32 ± 0.062	0.38 ± 0.06	23.7 ± 1.7	24.1 ± 1.7
4.09 ± 0.062	0.20 ± 0.05	26.0 ± 1.9	26.3 ± 1.9
3.85 ± 0.052	0.22 ± 0.05	38.7 ± 2.8	38.9 ± 2.8
3.61 ± 0.052	0.41 ± 0.08	53.0 ± 3.8	53.4 ± 3.9
3.36 ± 0.061	0.56 ± 0.11	52.5 ± 3.8	53.1 ± 3.8
3.12 ± 0.061	0.72 ± 0.11	35.0 ± 2.5	35.7 ± 2.6
2.97 ± 0.071	0.73 ± 0.09	30.6 ± 2.2	31.4 ± 2.1
2.88 ± 0.080	0.52 ± 0.10	27.4 ± 2.0	27.9 ± 2.0
2.82 ± 0.052	1.13 ± 0.13	28.9 ± 2.1	30.0 ± 2.0
2.57 ± 0.061	7.53 ± 0.64	39.5 ± 2.9	47.0 ± 3.1
2.38 ± 0.080	7.60 ± 0.62	31.7 ± 2.3	39.3 ± 2.6
2.07 ± 0.098	2.18 ± 0.20	20.2 ± 1.5	22.4 ± 1.5
1.99 ± 0.089	1.18 ± 0.12	19.2 ± 1.4	20.3 ± 1.4
1.85 ± 0.088	2.81 ± 0.25	19.5 ± 1.4	22.3 ± 1.5
1.63 ± 0.078	1.36 ± 0.20	22.1 ± 1.6	23.5 ± 1.7
1.41 ± 0.077	1.70 ± 0.17	22.7 ± 1.6	24.4 ± 1.6
1.19 ± 0.085	1.47 ± 0.23	18.8 ± 1.4	20.3 ± 1.5
1.06 ± 0.075	1.51 ± 0.15	15.5 ± 1.1	17.0 ± 1.1
0.90 ± 0.090	1.11 ± 0.13	20.6 ± 1.5	21.7 ± 1.5
0.75 ± 0.087	0.86 ± 0.13	47.4 ± 3.4	48.2 ± 3.2
0.71 ± 0.086	0.98 ± 0.27	46.6 ± 3.5	47.6 ± 3.6
0.69 ± 0.085	1.71 ± 0.37	55.4 ± 4.2	57.1 ± 4.2
0.58 ± 0.059	0.47 ± 0.32	80.0 ± 12.5	80.5 ± 12.6
0.43 ± 0.044	0.43 ± 0.39	46.2 ± 7.1	46.6 ± 7.2
0.34 ± 0.035	< 10 <sup>-3</sup>	8.8 ± 1.4	8.8 ± 1.4

ence of an additional resonance in this energy region. In particular, Fig. 10b presents data alongside possible excited states of <sup>12</sup>C, reinforcing the likelihood of a new resonance peak that warrants further investigation.

## 4 Conclusions

This study provides an evaluation of the p-11B nuclear reaction cross section over a proton energy range of 0.34 to 4.73 MeV, using a novel experimental setup featuring boron-coated targets produced via Pulsed Laser Deposition (PLD) and a monolithic silicon telescope for effective particle discrimination. The use of a two-stage detector was critical in enabling the separation of scattered protons from  $\alpha$  particles,

allowing for accurate measurements of  $\alpha$  spectra without the interference typically seen in single-stage detectors.

This capability is essential, especially in the low-energy region of the spectrum where scattered protons can overlap with the  $\alpha$  particle spectra. The obtained energy spectra show a strong agreement with prior studies, particularly at higher proton energies, pointing out that the experimental proton-alpha discrimination is crucial for the study of this complex reaction.

However, some discrepancies were observed at lower proton energies, particularly closed to the resonance peak identified in earlier studies. On the other hand, the results are generally consistent with the average values observed in other cross-section data available in the literature. These discrepancies highlight the sensitivity of the reaction cross section to precise energy calibration and the importance of further refining energy measurements in future experiments and the importance of assessing an experimental uncertainty on the obtained values.

One of the most significant findings in this study is the pronounced increase in the reaction cross section near 4.5 MeV, suggesting the possible existence of an additional resonance in this energy range. This observation is noteworthy, as previous studies lack data in this specific energy window, leaving this potential resonance largely unexplored. The presence of this resonance could have important implications for both theoretical models and practical applications of the p-11B reaction.

This work successfully demonstrates the use of a two-stage silicon telescope for accurate cross section measurements and particle discrimination in the p-11B fusion reaction. The results not only corroborate existing data at higher energies but also point to new areas for further investigation, particularly around the 4.5 MeV resonance. Additionally, refining proton beam energy calibration techniques will be crucial in resolving the observed discrepancies at lower energies and improving the overall accuracy of cross section measurements. Finally, it should be noted that the cross sections described in this work have been calculated by considering a single emission angle (60° in the laboratory frame): a complete and more comprehensive work should consider also other emission angles. For the same reason, the interpretation of the mono-energetic  $\alpha$  particle emission for certain energies needs a deeper understating corroborated with measurements for other angles. This will be matter of future work.

**Funding** Open access funding provided by Politecnico di Milano within the CRUI-CARE Agreement.

**Data Availability Statement** Data will be made available on reasonable request. [Author's comment: The datasets generated during and/or analysed during the current study are available from the corresponding author on reasonable request.]

**Code Availability Statement** This manuscript has no associated code/software. [Author's comment: Code/Software sharing not applicable to this article as no code/software was generated or analysed during the current study.]

**Open Access** This article is licensed under a Creative Commons Attribution 4.0 International License, which permits use, sharing, adaptation, distribution and reproduction in any medium or format, as long as you give appropriate credit to the original author(s) and the source, provide a link to the Creative Commons licence, and indicate if changes were made. The images or other third party material in this article are included in the article's Creative Commons licence, unless indicated otherwise in a credit line to the material. If material is not included in the article's Creative Commons licence and your intended use is not permitted by statutory regulation or exceeds the permitted use, you will need to obtain permission directly from the copyright holder. To view a copy of this licence, visit <http://creativecommons.org/licenses/by/4.0/>.

## References

- D.K. Yoon, J.Y. Jung, T.S. Suh, *Appl. Phys. Lett.* **105**, (2014) <https://doi.org/10.1063/1.4903345>
- J.Y. Jung, D.K. Yoon, B. Barraclough, H.C. Lee, T.S. Suh, B. Lu, *Oncotarget* **8**, (2017) <https://doi.org/10.18632/oncotarget.15700>
- M.S. Kim, M. Wai-Ming Law, S.K. Djeng, H.B. Shin, M.G. Choi, Y.J. Kim, B.Y. Choe, T.S. Suh, D.K. Yoon, *AIP Adv.* **9**, (2019) <https://doi.org/10.1063/1.5124322>
- G.A.P. Cirrone, L. Manti, D. Margarone, G. Petringa, L. Giuffrida, A. Minopoli, A. Picciotto, G. Russo, F. Cammarata, P. Pisciotto, F.M. Perozziello, F. Romano, V. Marchese, G. Milluzzo, V. Scuderi, G. Cuttone, G. Korn, *Sci. Rep.* **8**, (2018) <https://doi.org/10.1038/s41598-018-19258-5>
- P. Bláha, C. Feoli, S. Agosteo, M. Calvaruso, F.P. Cammarata, R. Catalano, M. Ciocca, G.A.P. Cirrone, V. Conte, G. Cuttone, A. Facioetti, G.I. Forte, L. Giuffrida, G. Magro, D. Margarone, L. Minafra, G. Petringa, G. Pucci, V. Ricciardi, E. Rosa, G. Russo, L. Manti, *Front. Oncol.* **11**, (2021) <https://doi.org/10.3389/fonc.2021.682647>
- A. Michaelidesová, P. Kundrát, O. Zahradnicek, I. Danilova, K. Pachnerova Brabcova, J. Vachelova, J. Vilimovský, M. David, V. Vondracek, M. Davidkova, *Sci. Rep.* **14**, (2024) <https://doi.org/10.1038/s41598-024-69370-y>
- G.A.P. Cirrone, G. Petringa, A. Attili, D. Chiappara, L. Manti, V. Bravatà, D. Margarone, M. Mazzocco, G. Cuttone, *RAD Assoc. J.* **3**, (2019) <https://doi.org/10.21175/radj.2018.03.025>
- T.A. Chiniforush, A. Hadadi, Y. Kasesaz, Y. Sardjono, *Appl. Radiat. Isot.* **170**, (2021) <https://doi.org/10.1016/j.apradiso.2021.109596>
- P. Kundrát, K.P. Brabcová, A.J. Michaelidesová, O. Zahradníček, I. Danilová, V. Štěpán, Z. Jamborová, M. Davidková, *Radiat. Prot. Dosimetry* **198**, (2022) <https://doi.org/10.1093/rpd/ncac093>
- D. Mazzucconi, D. Bortot, A. Pola, A. Fazzi, L. Cazzola, V. Conte, G. Cirrone, G. Petringa, G. Cuttone, L. Manti, S. Agosteo, *Phys. Med.* **89**, 226–231 (2021). <https://doi.org/10.1016/j.ejmp.2021.08.008>
- Z.A. Ganjeh, M.A. Mosleh-Shirazi, *Rad. Phys. Chem.* **214**, (2024) <https://doi.org/10.1016/j.radphyschem.2023.111289>
- D.C. Moreau, *Nucl. Fusion* **17**, (1977) <https://doi.org/10.1088/0029-5515/17/1/002>
- D. Margarone, J. Bonvalet, L. Giuffrida, A. Morace, V. Kantarelou, M. Tosca, D. Raffestin, P. Nicolai, A. Picciotto, Y. Abe, Y. Arikawa, S. Fujioka, Y. Fukuda, Y. Kuramitsu, H. Habara, D. Batani, *Appl. Sci.* **12**, (2022) <https://doi.org/10.3390/app12031444>
- V. Istokskaia, M. Tosca, L. Giuffrida, J. Psikal, F. Grepl, V. Kantarelou, S. Stancek, S. Di Siena, A. Hadjikyriacou, A. McIlvenny, Y. Levy, J. Huynh, M. Cimrman, P. Pleskunov, D. Nikitin, A. Choukourov, F. Belloni, A. Picciotto, S. Kar, M. Borghesi, A. Lucianetti, T. Mocek, D. Margarone, *Commun. Phys.* **6**, (2023) <https://doi.org/10.1038/s42005-023-01135-x>
- D. Batani, D. Margarone, F. Belloni, *Laser Part. Beams* (2023). <https://doi.org/10.1155/2023/9824024>
- I.E. Ochs, E.J. Kolmes, M.E. Mlodik, T. Rubin, N.J. Fisch, *Phys. Rev. E* **106**, (2022) <https://doi.org/10.1103/PhysRevE.106.055215>
- K. Ogawa, R.M. Magee, T. Tajima, H. Gota, P. McCarroll, I. Allfrey, H. Nuga, M. Isobe, M. Osakabe, *Nuclear Fusion* **64**, (2024) <https://doi.org/10.1088/1741-4326/ad6615>
- R.M. Magee, K. Ogawa, T. Tajima, I. Allfrey, H. Gota, P. McCarroll, S. Ohdachi, M. Isobe, S. Kamio, V. Klumper, H. Nuga, M. Shoji, S. Ziaei, M.W. Binderbauer, M. Osakabe, *Nat. Commun.* **14**, (2023) <https://doi.org/10.1038/s41467-023-36655-1>
- O. Beckman, T. Huus, A. Zupančič, *Phys. Rev.* **91**, 606 (1953). <https://doi.org/10.1103/PhysRev.91.606>
- G. Dearnaley, G.A. Dissanaikie, A.P. French, G. Lindsay Jones, *Phys. Rev.* **108**, (1957) 743–753 <https://doi.org/10.1103/PhysRev.108.743>
- M. Munch, O.S. Kirsebom, J.A. Swartz, H. Fynbo, *Eur. Phys. J. A* **56**, 1–7 (2020). <https://doi.org/10.1140/epja/s10050-019-00016-8>
- G.D. Symons, P.B. Treacy, *Nucl. Phys.* **46**, 93–107 (1963). [https://doi.org/10.1016/0029-5582\(63\)90567-4](https://doi.org/10.1016/0029-5582(63)90567-4)
- R.E. Segel, S.S. Hanna, R.G. Allas, *Phys. Rev.* **139**, B818 (1965). <https://doi.org/10.1103/PhysRev.139.B818>
- D. Kamke, J. Krug, *Zeitschrift Für Phys.* **201**, 301–322 (1967). <https://doi.org/10.1007/BF01326819>
- J.M. Davidson, H.L. Berg, M.M. Lowry, M.R. Dwarakanath, A.J. Sierk, P. Batay-Csorba, *Nucl. Phys. A* **315**, 253–268 (1979). [https://doi.org/10.1016/0375-9474\(79\)90647-X](https://doi.org/10.1016/0375-9474(79)90647-X)
- H.W. Becker, C. Rolfs, H.P. Trautvetter, *At. Nucl.* **327**, 341–355 (1987)
- J. Liu, X. Lu, X. Wang, W.K. Chu, *Nucl. Instrum. Methods Phys. Res. B* **190**, 107–111 (2002). [https://doi.org/10.1016/S0168-583X\(01\)01272-1](https://doi.org/10.1016/S0168-583X(01)01272-1)
- M.C. Spraker, M.W. Ahmed, M.A. Blackston, N. Brown, R.H. France, S.S. Henshaw, B.A. Perdue, R.M. Prior, P.N. Seo, S. Stave, H.R. Weller, *J. Fusion Energy* **31**, 357–367 (2012). <https://doi.org/10.1007/s10894-011-9473-5>
- M.H. Sikora, H.R. Weller, *J. Fusion Energy* **35**, 538–543 (2016). <https://doi.org/10.1007/s10894-016-0069-y>
- S. Taskaev, V. Bessmeltsev, M. Bikchurina, T. Bykov, D. Kasatov, I. Kolesnikov, A. Nikolaev, E. Oks, G. Ostreimov, S. Savinov, A. Shuklina, E. Sokolova, G. Yushkov, *Nucl. Instrum. Methods Phys. Res. B* **555**, 165490 (2024). <https://doi.org/10.1016/j.nimb.2024.165490>
- F. Borchers, H. De Jong, J. Krug, E. Kuhlmann, *Nucl. Phys. A* **405**, 141–158 (1983). [https://doi.org/10.1016/0375-9474\(83\)90328-7](https://doi.org/10.1016/0375-9474(83)90328-7)
- W. Buck, F. Hoyler, A. Stäbler, G. Staudt, H.V. Klapdor, H. Oeschler, *Nucl. Phys. A* **398**, (1983) [https://doi.org/10.1016/0375-9474\(83\)90482-7](https://doi.org/10.1016/0375-9474(83)90482-7)
- Experimental nuclear reaction data (EXFOR), available at: [www-nds.iaea.org/exfor](http://www-nds.iaea.org/exfor), (n.d.)
- M. Chiari, L. Giuntini, P.A. Mandò, N. Taccetti, *Nucl. Instrum. Methods Phys. Res. B Beam Interact. with Mater. Atoms.* (2001) [https://doi.org/10.1016/S0168-583X\(01\)00787-X](https://doi.org/10.1016/S0168-583X(01)00787-X)
- F.A. Geser, M. Valente, *Radiat. Phys. Chem.* **167**, (2020) <https://doi.org/10.1016/j.radphyschem.2019.03.028>
- M. Kuhlwein, K. Lytje, H.O.U. Fynbo, A. Gad, E. Jensen, O.S. Kirsebom, M. Munch, J. Refsgaard, K. Riisager, *Phys. Lett. B* **825**, (2022) <https://doi.org/10.1016/j.physletb.2021.136857>

37. J. Ferrari, A. Sala, P.R. Fassio, A. Ranft, FLUKA: A multi-particle transport code (Program version 2005), Cern-2005-010. (2005)
38. T.T. Böhlen, F. Cerutti, M. Chin, A. Fassò, A. Ferrari, P.G. Ortega, A. Mairani, P.R. Sala, G. Smirnov, V. Vlachoudis, Nucl. Data Sheets (2014). <https://doi.org/10.1016/j.nds.2014.07.049>
39. S.V. Putvinski, D.D. Ryutov, P.N. Yushmanov, Nucl. Fusion **59**, (2019) <https://doi.org/10.1088/1741-4326/ab1a60>
40. A. Tentori, F. Belloni, Nucl. Fusion **63**, 86001 (2023). <https://doi.org/10.1088/1741-4326/acda4b>
41. D. Mazzucconi, D. Vavassori, D. Dellasega, F.M. Airaghi, S. Agosteo, M. Passoni, A. Pola, D. Bortot, Radiat. Phys. Chem. **204**, (2023) <https://doi.org/10.1016/j.radphyschem.2022.110727>
42. K.L. Laursen, H.O.U. Fynbo, O.S. Kirsebom, K.S. Madsbøll, K. Riisager, Eur. Phys. J. A **52**, (2016) <https://doi.org/10.1140/epja/i2016-16271-2>
43. W. Lv, H. Duan, J. Liu, Nuc. Phys. A **1025**, 122490 (2022). <https://doi.org/10.1016/j.nuclphysa.2022.122490>
44. J.H. Kelley, J.E. Purcell, C.G. Sheu, Nucl. Phys. A **968**, 71–253 (2017). <https://doi.org/10.1016/j.nuclphysa.2017.07.015>
45. J.D. Bronson, W.D. Simpson, W.R. Jackson, G.C. Phillips, Nucl. Phys. **68**, 241–269 (1965). [https://doi.org/10.1016/0029-5582\(65\)90643-7](https://doi.org/10.1016/0029-5582(65)90643-7)
46. Y. Chanut, J.N. Scheurer, R. Ballini, J.L. Quebert, Y. Flamant, C. Perrin, Nucl. Phys. A **194**, 523–534 (1972). [https://doi.org/10.1016/0375-9474\(72\)90999-2](https://doi.org/10.1016/0375-9474(72)90999-2)
47. M. Bogovac, S. Fazinić, M. Jakšić, M. Lattuada, D. Miljanić, N. Soić, C. Spitaleri, M. Zadro, Fiz. B **4**, 229–236 (1995)
48. M. Munch, H. Fynbo, Eur. Phys. J. A **54**, 1–8 (2018). <https://doi.org/10.1140/epja/i2018-12577-3>
49. S. Stave, M.W. Ahmed, R.H. France, S.S. Henshaw, B. Müller, B.A. Perdue, R.M. Prior, M.C. Spraker, H.R. Weller, Phys. Lett. B **696**, 26–29 (2011). <https://doi.org/10.1016/j.physletb.2010.12.015>
50. D. Dellasega, V. Russo, A. Pezzoli, C. Conti, N. Lecis, E. Besozzi, M. Beghi, C.E. Bottani, M. Passoni, Mater. Des. **134**, (2017) <https://doi.org/10.1016/j.matdes.2017.08.025>
51. A. Pazzaglia, A. Maffini, D. Dellasega, A. Lamperti, M. Passoni, Mater. Charact. **153**, 92–102 (2019). <https://doi.org/10.1016/j.matchar.2019.04.030>
52. A. Pola, D. Bortot, D. Mazzucconi, A. Fazzi, S. Galer, K.J. Kirkby, M.J. Merchant, H. Palmans, S. Agosteo, Radiat. Meas. **133**, 106296 (2020). <https://doi.org/10.1016/j.radmeas.2020.106296>